Schweizerischer Erdbebendienst
Service Sismologique Suisse
Servizio Sismico Svizzero
Swiss Seismological Service

ETH zürich

SITE CHARACTERIZATION REPORT

SBGN: Bergün/Bravuogn (GR) - Schule

Manuel Hobiger, Paolo Bergamo, Donat Fäh

Last Modification: 16/04/2020

Schweizerischer Erdbebendienst (SED)
Service Sismologique Suisse
Servizio Sismico Svizzero
Servizi da Terratrembels Svizzer

ETH Zürich
Sonneggstrasse 5
8092 Zürich
Schweiz
manuel.hobiger@sed.ethz.ch

Contents

Summary

The free-field strong-motion station SBGN was built in Bergün/Bravuogn (GR) next to the building that houses the administration and the school. We performed a passive seismic array measurement with two array configurations to characterize the soil underneath the station.
The measurements show that the fundamental frequency of the structure beneath the station is about 3 Hz. The array measurements were analyzed with different techniques, namely 3-component HRFK, WaveDec and SPAC. All techniques gave similar dispersion curves. The dispersion curves for the fundamental modes of both Love and Rayleigh waves could be retrieved from around 2.9 to 51.7 Hz and 3.6 to 41.5 Hz, respectively.
The joint inversion of Love and Rayleigh wave dispersion curves and the Rayleigh wave ellipticity angle showed that the structure can be explained by models with two main interfaces at around 2.5 m and 80 m depth, where the latter corresponds to H800. The V_{S30} of the best models is about 638 m/s, corresponding to soil class B in both EC8 and SIA261.

1 Introduction

In the framework of the second phase of the Swiss Strong Motion Network (SSMNet) renewal project, a new station was planned in Bergün/Bravuogn (GR) to replace the old station SBET, which was located in an electrical cabinet on the Albula pass road south of Bergün. The area behind the building housing the school and the public administration was selected as the best site. The new station, called SBGN, went operational on 15 July 2015. The location of the station is shown in Fig. 1.

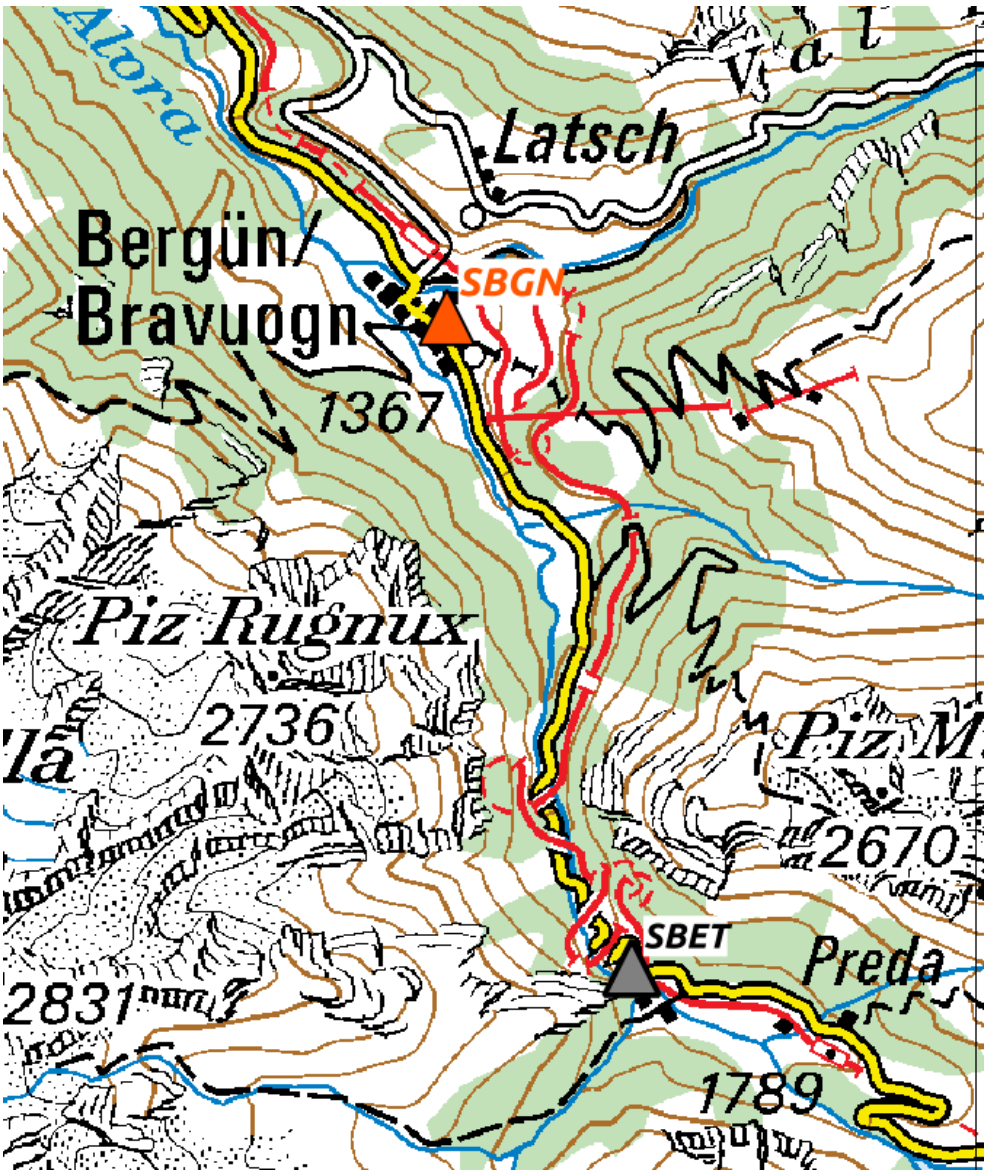

Figure 1: Map showing the location of station SBGN and the old station SBET in Bergün.

2 Geological setting

A geological map of the surroundings of station SBGN is shown in Fig. 2. The station is located on the transition from alluvial deposits of the Albula Valley to moraine. According to the map, some stations of the passive array measurement were located on alluvial deposits, some on moraine.

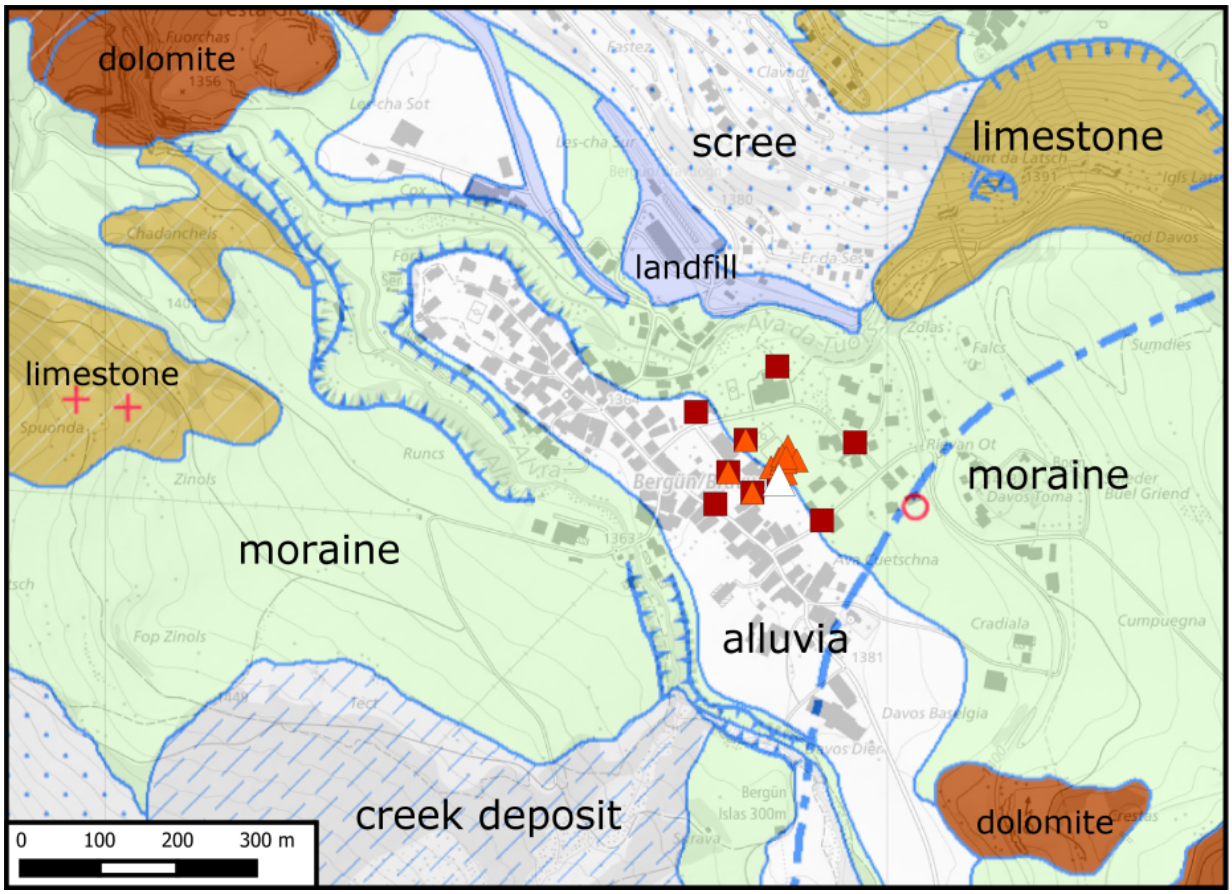

Figure 2: Geological map of the area around station SBGN. According to the geological atlas (1:25000), station SBGN lies on the transition zone between alluvial deposits and moraine. ©2020 swisstopo (JD100042)

3 Site characterization measurements

3.1 Data set

In order to characterize the local underground structure around station SBGN, passive seismic array measurements were carried out on 10 October 2015. The layout of the seismic measurements is shown in Fig. 3.
Two array measurements were performed (see Table 1 for the main characteristics). The first array consisted of 14 running stations. Two additional stations were deployed, but not working. The first array was planned to consist of two inner rings of five stations each around a central station, with ring radii of 5 m and 18 m, respectively. In addition, another five stations were planned on a ring with its center shifted towards the southwest, located inside the school building. This ring had a planned radius of 36 m. One of the stations of this array, SBGN01, was located close to the permanent station SBGN. The final minimum and maximum inter-station distances in the array were 4.9 m and 88.9 m, respectively. The names of the stations of the first array are composed of "SBGN" followed by a two-digit number (01 to 03, 05 to 12, 22, 29, 30). The seismic stations consisted of Lennartz 3C 5 s sensors connected to Quanterra Q330 digitizers.
The second array consisted of 9 stations. For this array, four stations located on the third ring of the first array were kept. Another ring of five stations with a radius of around 100 m was placed around these stations. The minimum and maximum inter-station distances of the second array were 38.0 and 212.5 m, respectively. The station names of the stations in the second array are composed of "SBGN" and a two-digit number between 51 and 62 (51, 53, 55, 56, 58, 59, 60, 61, 62).
The station locations have been measured by a differential GPS system (Leica Viva GS10) with a precision better than 5 cm for all stations.

Table 1: List of the passive seismic array measurements in Bergün.

Array name	Number of sensors	Minimum interstation distance [m]	Maximum interstation distance [m]	Recording time [s]
1	14	4.9	88.9	7200
2	9	38.0	212.5	8100

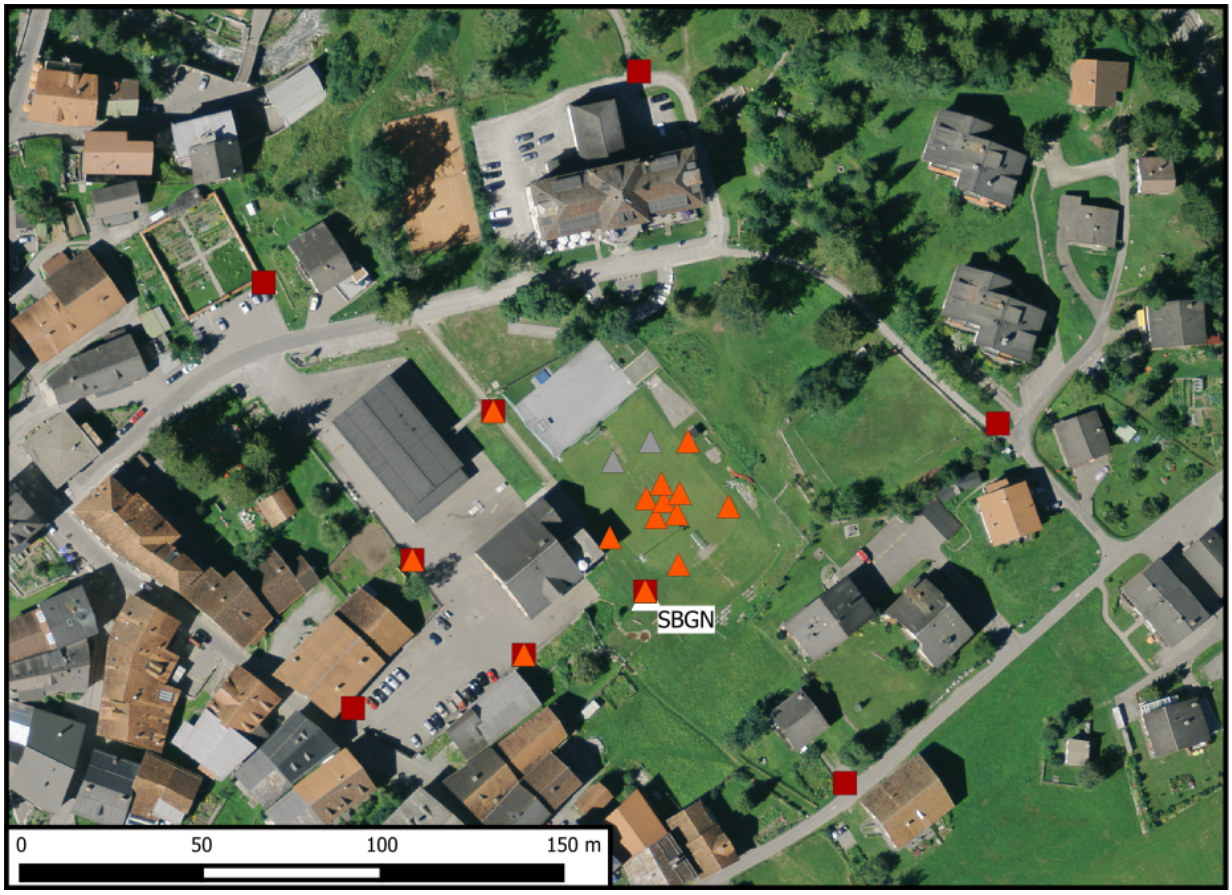

Figure 3: Layout of the array measurements around station SBGN. The location of SBGN is indicated by the white triangle, the locations of the stations for the passive seismic measurement by the orange triangles (first array) and red squares (second array). The two gray triangles show the locations of the two sensors which were not recording. ©2020 swisstopo (JD100042)

3.2 H/V and RayDec ellipticity curves

Figure 4 shows the H/V curves determined with the time-frequency analysis method (Fäh et al., 2009) for all stations of both passive arrays. All curves are similar and show a broad peak between 2 and 3.2 Hz. At frequencies above 10 Hz, there is more variability in the curves, related with shallow variations in the underground structure. One curve is significantly lower than the other curves below 1 Hz. This curve belongs to the northwesternmost station, which was located close to the cemetery. Another curve is lower than the others around the peak. This curve belongs to the northernmost array station, located close to the Kurhaus. In this area, the deeper underground structure may be different from the central areas of the array.
The RayDec technique (Hobiger et al., 2009) is supposed to eliminate the contributions of other wave types than Rayleigh waves and give a better estimate of the ellipticity than the classical H/V technique. The RayDec ellipticity curves for all stations of the array measurements are shown in Fig. 4 and are similar to the H/V curves. Station SBGN01, the station closest of SBGN, serves as a reference and will be used for the inversion.
The amplitudes of both the H/V and the RayDec peaks are not especially high, with values between 2 and 3 for H/V and up to 4 for RayDec. However, the trough at frequencies of around 5 Hz is very pronounced with low values of around 0.5 for H/V and RayDec. We can interpret this as a hint for singularities in the ellipticity curve. In that case, the peak would go towards infinity and the trough towards zero. At frequencies below the peak and above the trough, the Rayleigh wave particle motion would then be retrograde. Between peak and trough, it would be prograde. The WaveDec processing (see section 3.5) will give more insight in the particle motion.

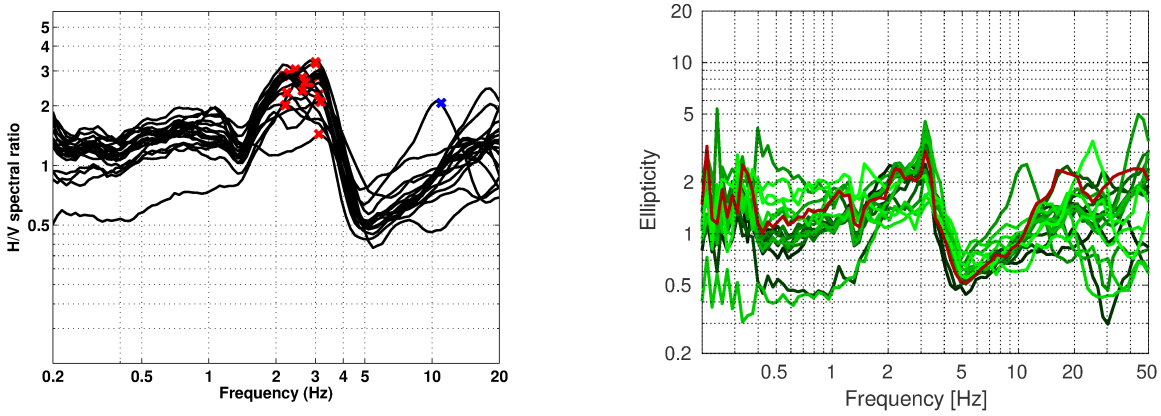

Figure 4: Left: Overview of the H/V measurements for the different stations of both array measurements. Right: RayDec ellipticities for all measurement stations. The red curve corresponds to SBGN01, the station located closest of the permanent station SBGN.

3.3 Polarization analysis

The polarization analysis was performed according to Burjánek et al. (2010) and Burjánek et al. (2012). The results for all stations of the array are similar. Only the results for SBGN01, the station closest to SBGN, are shown here.
There is no preferential linear particle polarization visible and we do not see indications for 2-dimensional polarization effects.

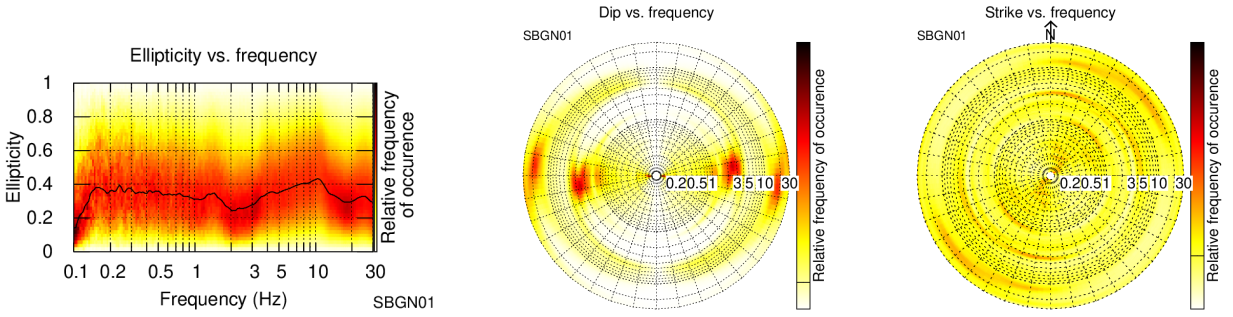

Figure 5: Polarization analysis of station SBGN01.

3.4 3-component high-resolution FK

The results of the 3-component high-resolution FK analysis (Poggi and Fäh, 2010) are shown in Fig. 6 (dispersion curves) and Fig. 7 (ellipticity curves). On the transverse component, corresponding to Love waves, we can clearly identify a dispersion curve for array 1 from 7.2 up to 51.7 Hz and for array 2 from 2.9 to 8.7 Hz, covering the entire accessible frequency range for each array.
On the vertical component, corresponding to Rayleigh waves, we can clearly identify one mode between 6.3 and 45.1 Hz for array 1 and between 3.6 and 8.3 Hz for array 2, spanning almost the entire accessible frequency range. On the radial component, also related with Rayleigh waves, the results are similar for array 1, where, in addition to the fundamental mode, a higher mode can be retrieved. For array 2, the result is more scattered than for the vertical component.
The corresponding ellipticity curves of these modes (Fig. 7) are mostly flat and show signs of an ellipticity peak below the lowest accessible frequency.

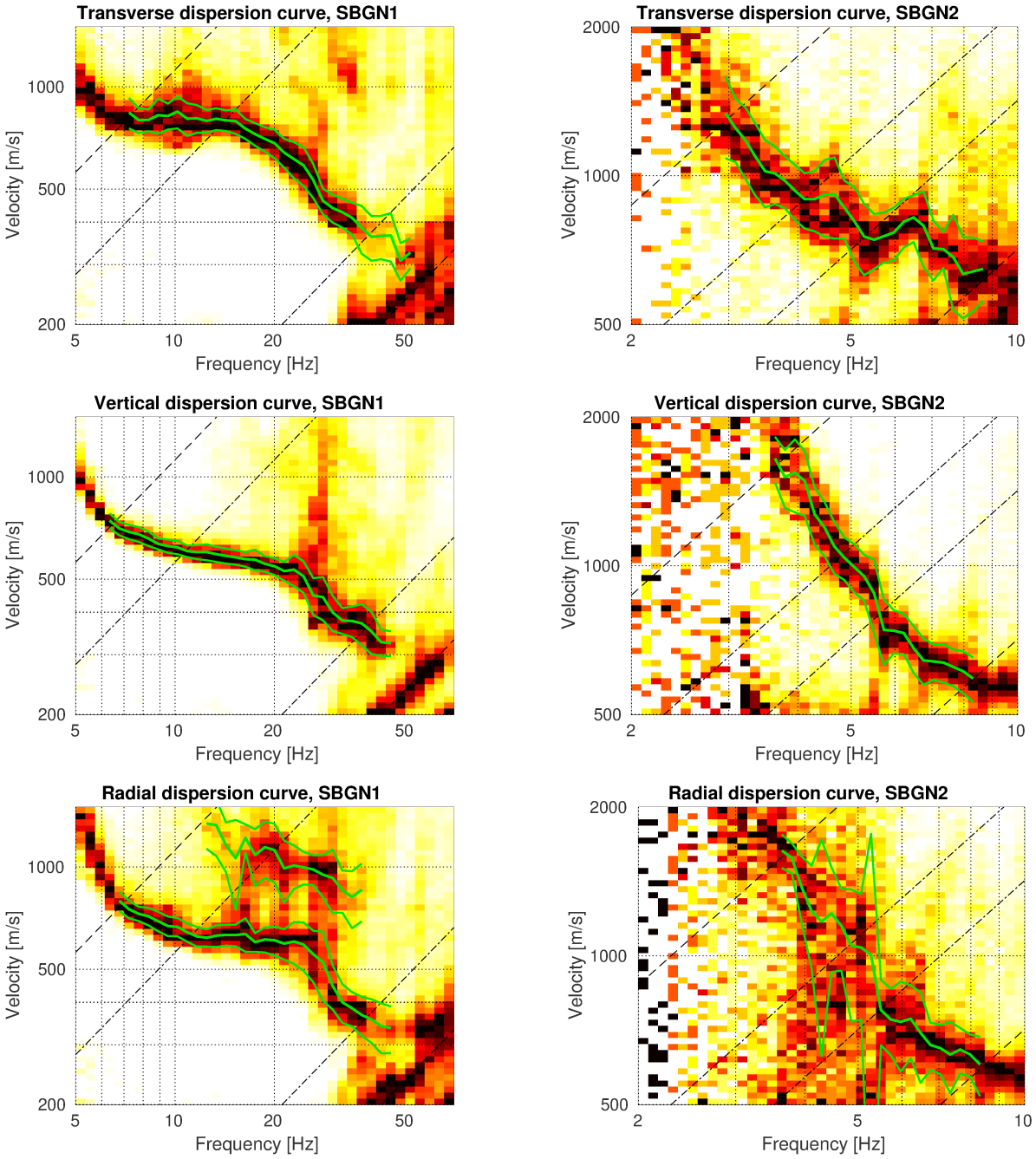

Figure 6: Dispersion curves obtained with the 3-component HRFK algorithm (Poggi and Fäh, 2010). From top to bottom, the dispersion curves for the transverse, vertical and radial components are shown for array 1 (left column) and array 2 (right column). The dashed and dotted black lines are the array resolution limits. The solid green lines are picked from the data, where the inner line indicates the picked values and the two outer lines the standard deviation.

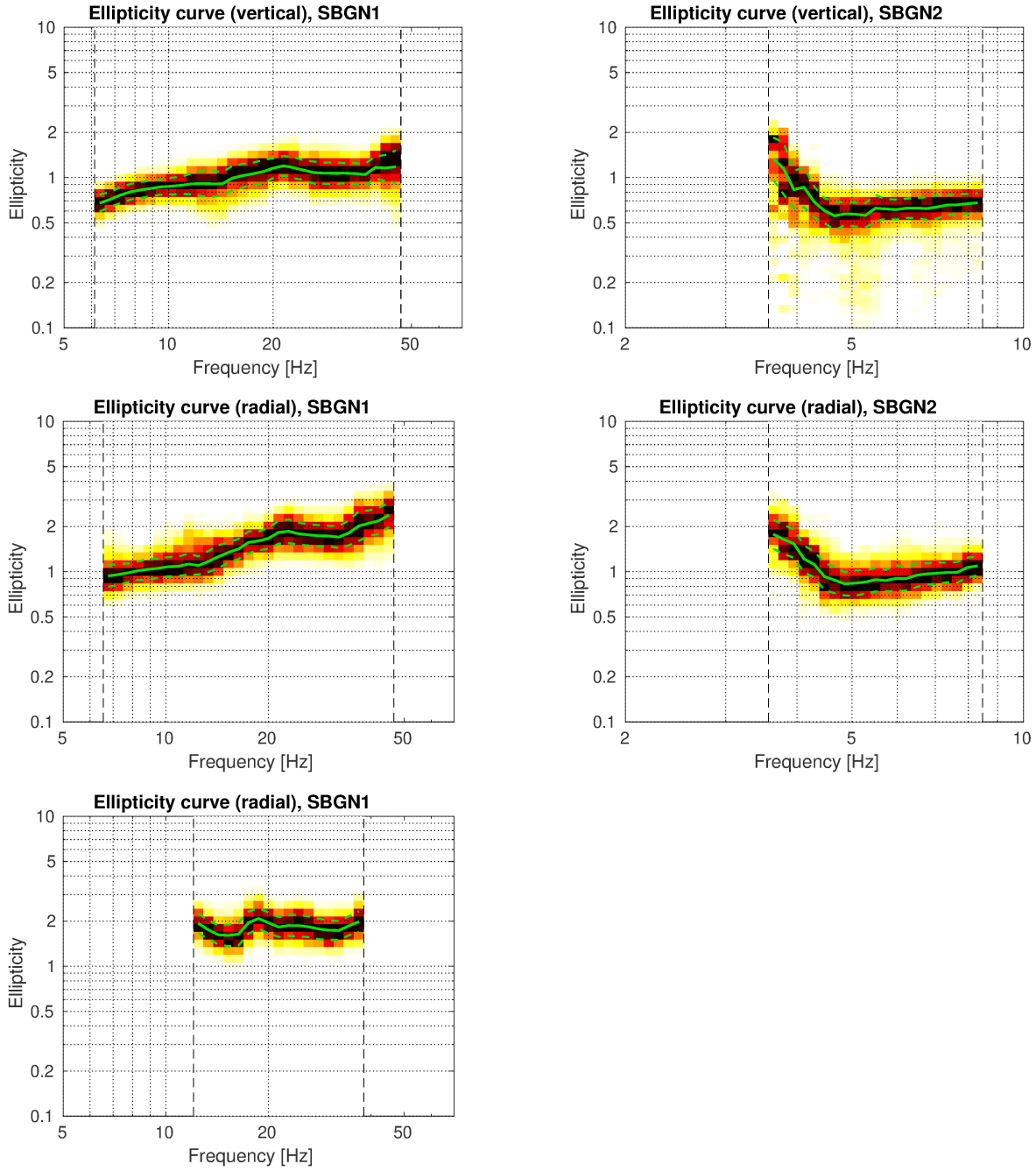

Figure 7: Ellipticity curves obtained with the 3-component HRFK algorithm (Poggi and Fäh, 2010) corresponding to the picked dispersion curves on the vertical and radial components for array 1 (left column) and array 2 (right column).

3.5 WaveDec

The results of the WaveDec (Maranò et al., 2012) processing are shown in Figs 8 and 9. This technique estimates the properties of single or multiple waves simultaneously with a wave field decomposition approach. In order to improve the results, the parameter γ, which modifies the sharpness of the wave property estimation, has been tuned. Here, a value of $\gamma = 0.2$ was used, corresponding to a predominantly maximum likelihood estimation.
The Love wave dispersion curve for array 1 is not well retrieved at lower frequencies and was only picked between 18.0 and 49.4 Hz. For array 2, the result is clearer and the curve was picked between 2.8 and 8.1 Hz.
The Rayleigh wave dispersion curve is retrieved between 6.5 and 57.7 Hz for array 1 and, less clearly, between 3.7 and 7.7 Hz for array 2. The ellipticity angles for the picked Rayleigh wave dispersion curves are negative for array 1 up to a frequency of around 50 Hz, where a change to prograde may be present. For array 2, the ellipticity angle is positive for frequencies below 4.5 Hz, indicating prograde particle motion, and negative above.

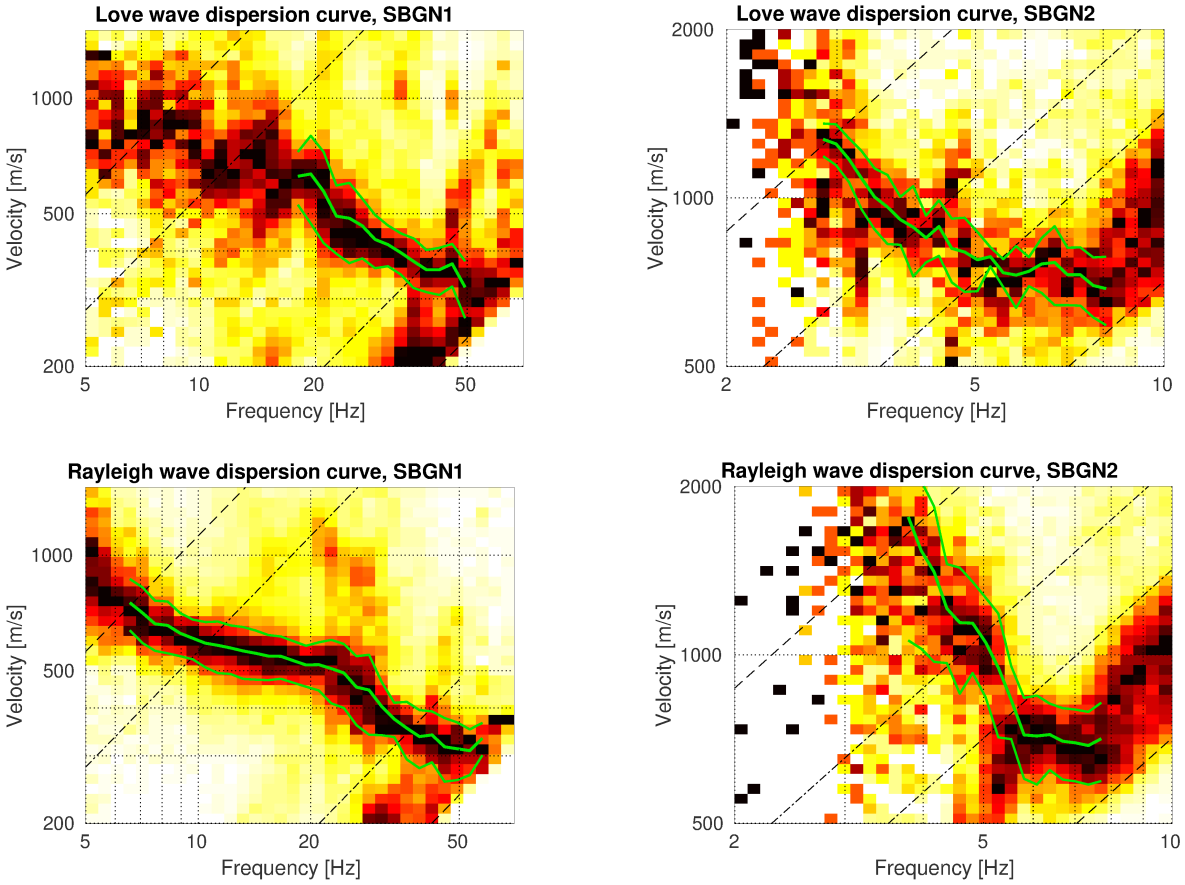

Figure 8: Love (top line) and Rayleigh (bottom line) wave dispersion curves obtained with the WaveDec technique (Maranò et al., 2012) for array 1 (left) and array 2 (right). The dashed lines indicate the theoretical array resolution limits.

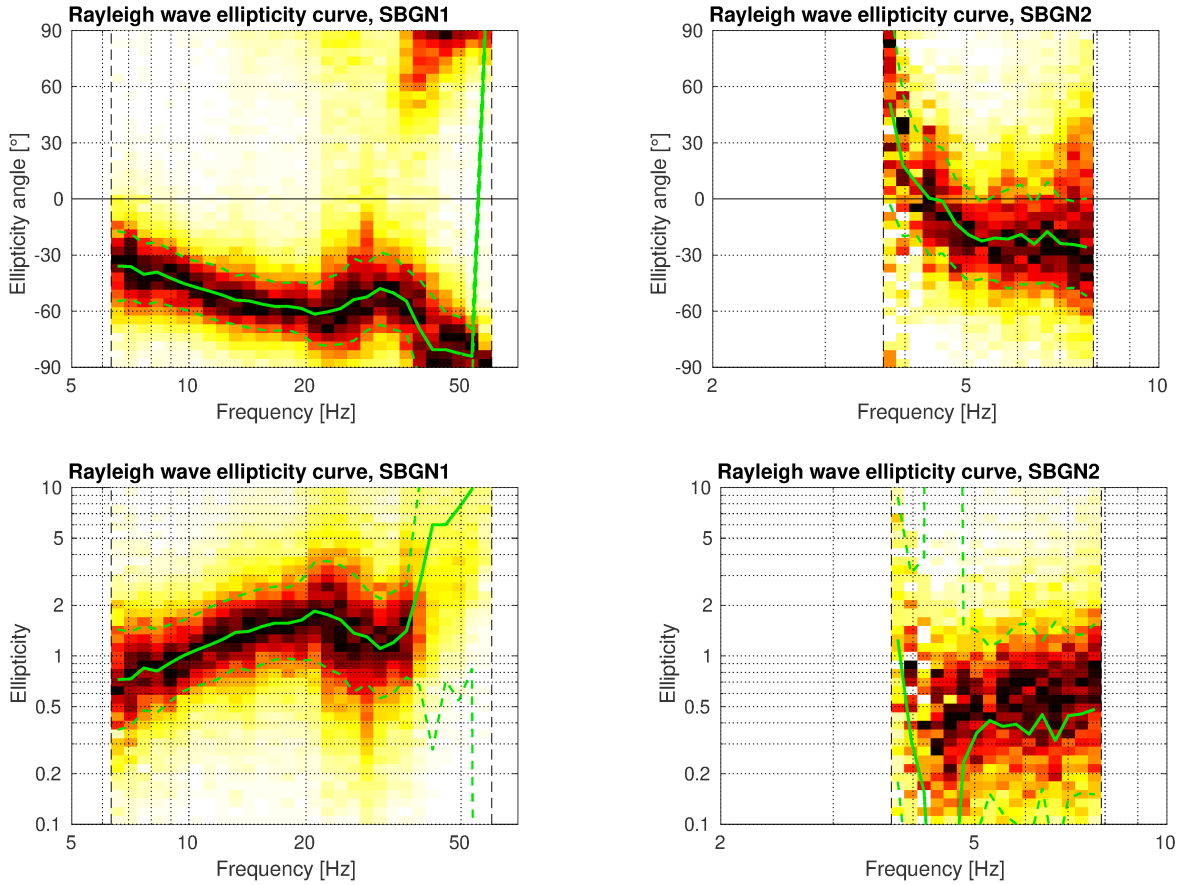

Figure 9: Rayleigh wave ellipticity curves obtained with the WaveDec technique (Maranò et al., 2012). Top line: Rayleigh wave ellipticity angles obtained using array 1 (left) and array 2 (right). Bottom line: Rayleigh wave ellipticity curve, i.e. the absolute value of the tangent of the ellipticity angle, for the curve of array 1 (left) and array 2 (right).

3.6 SPAC

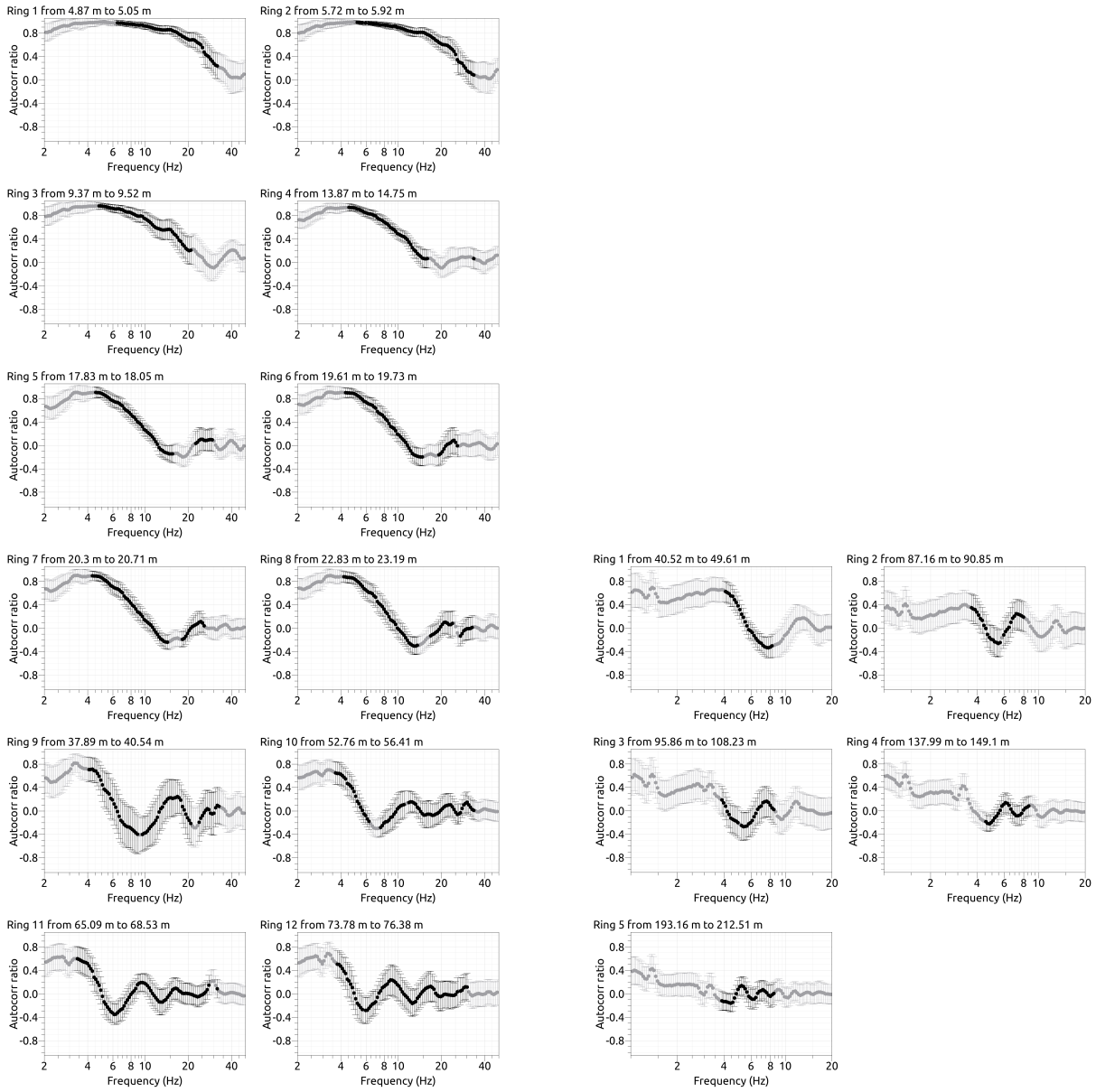

Figure 10: SPAC curves for array 1 (left) and array 2 (right). The black data points contributed to the dispersion curve estimation.

The SPAC (Aki, 1957) curves of the vertical components have been calculated using the M-SPAC (Bettig et al., 2001) technique implemented in geopsy. Rings with different radius ranges had been defined previously and for all station pairs with distance inside this radius range, the cross-correlation was calculated over a wide frequency range. These cross-correlation curves are averaged for all station pairs of the respective ring and give the SPAC curves. The rings are defined in such a way that at least three station pairs contribute and that their connecting vectors have a good directional coverage.
The SPAC curves for all defined rings are shown in Fig. 10. The black points indicate the data values which contributed to the final dispersion curve estimation, which was obtained with the function `spac2disp` of the geopsy package. These resulting dispersion curves are shown in Fig. 11.
The calculated SPAC curves have the shape of the theoretical Bessel functions. The retrieved Rayleigh wave dispersion curves range from 3.6 to 30.6 Hz for array 1 and from 3.7 to 8.0 Hz for array 2.

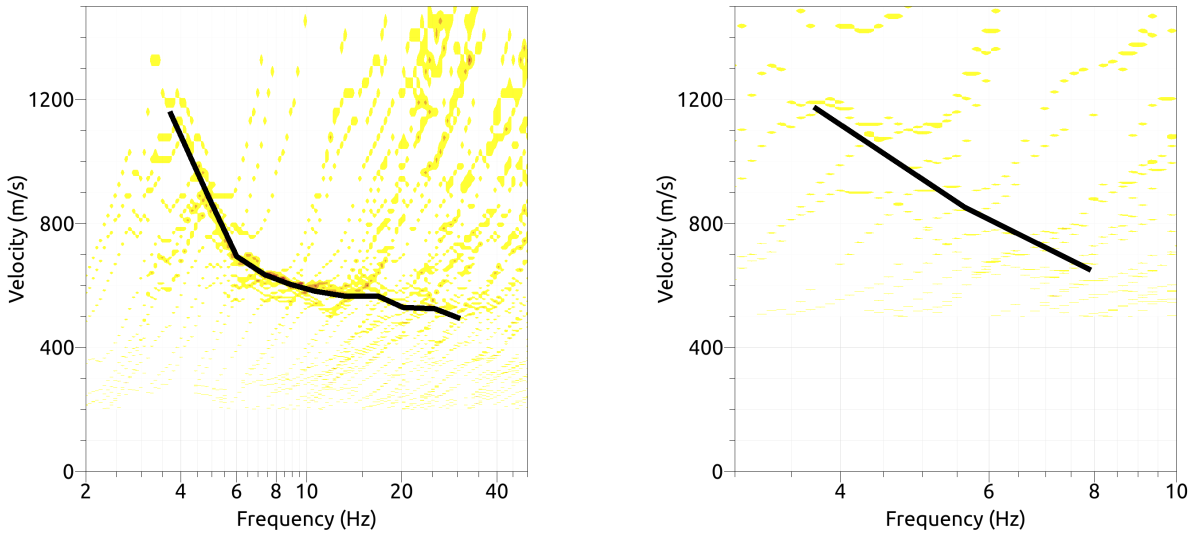

Figure 11: Resulting Rayleigh wave velocities for array 1 (left) and array 2 (right). The black line corresponds to the picked dispersion curve.

3.7 Summary

Fig. 12 gives an overview of the dispersion and ellipticity curves determined by the different methods.
For Love waves, the HRFK and WaveDec results for the respective arrays are in good overall agreement. In the transition area between both arrays, the curve from array 2 has lower velocities than the one for array 1 at frequencies above 7 Hz. It might be possible that the first higher mode influences the measurement with array 1 here. Combining both arrays, we can attribute a dispersion curve from 2.9 to 51.7 Hz.
For the Rayleigh waves, there is a very good agreement between the different methods. The radial HRFK curve of array 1 shows slightly higher velocity values and also shows a higher mode, but its attribution is unclear. At low frequencies, SPAC shows systematically lower velocities. Combining the different methods, we can attribute a continuous dispersion curve for the fundamental mode from 3.6 to 45.1 Hz.
The ellipticity curves retrieved using the different methods are in qualitative agreement. The single-station ellipticity curve determined with RayDec is the only one to cover frequencies lower than 4 Hz. It shows a broad peak between 2 and 3.5 Hz and a trough at around 5 Hz. At higher frequencies, RayDec shows another peak between 15 and 20 Hz. WaveDec shows a singular trough at about 4.5 Hz for array 2. The WaveDec curve for array 1 is in good agreement with the RayDec curve if we take into account that the RayDec curve is a single-station measurement and the WaveDec curve an average over the whole array.
The RayDec curve was transformed to ellipticity angle by using the arctan function. As we cannot distinguish between prograde and retrograde particle motion with a single-station method, we account for both possibilities and the RayDec (and HRFK) curves are represented twice, once for each sense of rotation. In the ellipticity angle representation, the WaveDec curve of array 2 shows prograde particle motion below 4.5 Hz and retrograde particle motion above. The WaveDec curve of array 1 shows retrograde particle motion up to 50 Hz. These results indicate that, first, the ellipticity peak at around 3 Hz has to correspond to a singularity with retrograde particle motion below and prograde particle motion above and, second, that there is a trough at around 4.5 Hz, where the particle motion changes back to retrograde.

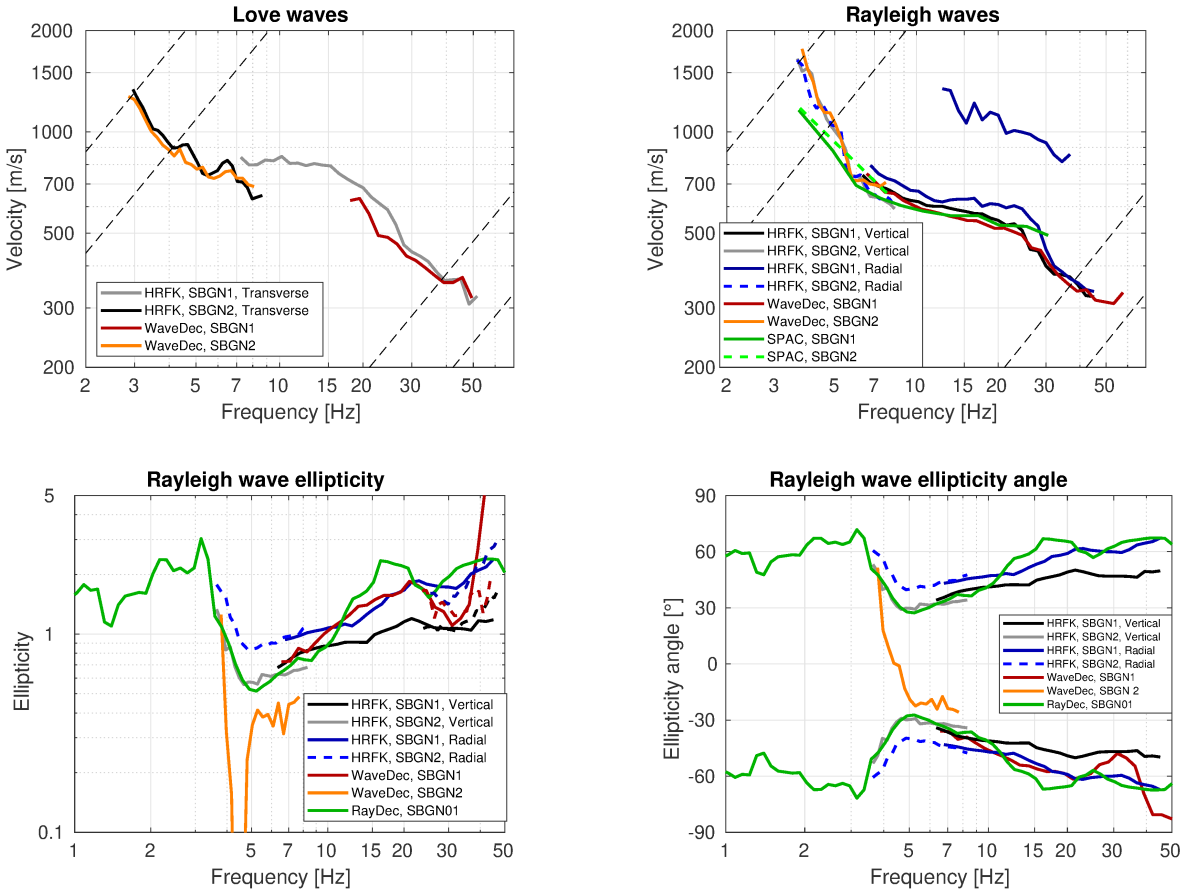

Figure 12: Overview of the Love and Rayleigh wave dispersion curves as well as the ellipticity and ellipticity angle curves for both arrays. The dashed lines indicate the theoretical resolution limits of array 1 (high frequencies) and array 2 (low frequencies). The RayDec ellipticity curve corresponds to station SBGN01, the closest station to the permanent station SBGN.

4 Data inversion

4.1 Inversion targets

We performed inversions using the Love and Rayleigh wave dispersion curves together with the Rayleigh wave ellipticity angle as inversion targets. For the dispersion curves, the HRFK dispersion curves were used for both Love and Rayleigh waves. It was tested if the Love wave dispersion curve of array 1 between 7 and 15 Hz might correspond to the first higher mode, but it was impossible to fit it together with the Rayleigh wave dispersion curve. Therefore, the Love wave dispersion curves were used as fundamental mode. The part of the Love wave dispersion curve above 5.3 Hz from array 2 was disregarded to allow a smooth transition between both parts of the dispersion curve. For Rayleigh waves, the two dispersion curves determined on the vertical component by HRFK were used.
For the ellipticity angle, a part of the RayDec curve below 2.1 Hz was used, assuming retrograde particle motion, and a part of the RayDec curve above 3.2 Hz, assuming prograde particle motion. In this way, the fundamental frequency of the site was not completely fixed, but the presence of a singularity was forced. The RayDec data was combined with parts of the WaveDec ellipticity angles for arrays 1 and 2.
The details of the inversion targets are indicated in Table 2 and the corresponding curves are shown in Fig. 13.

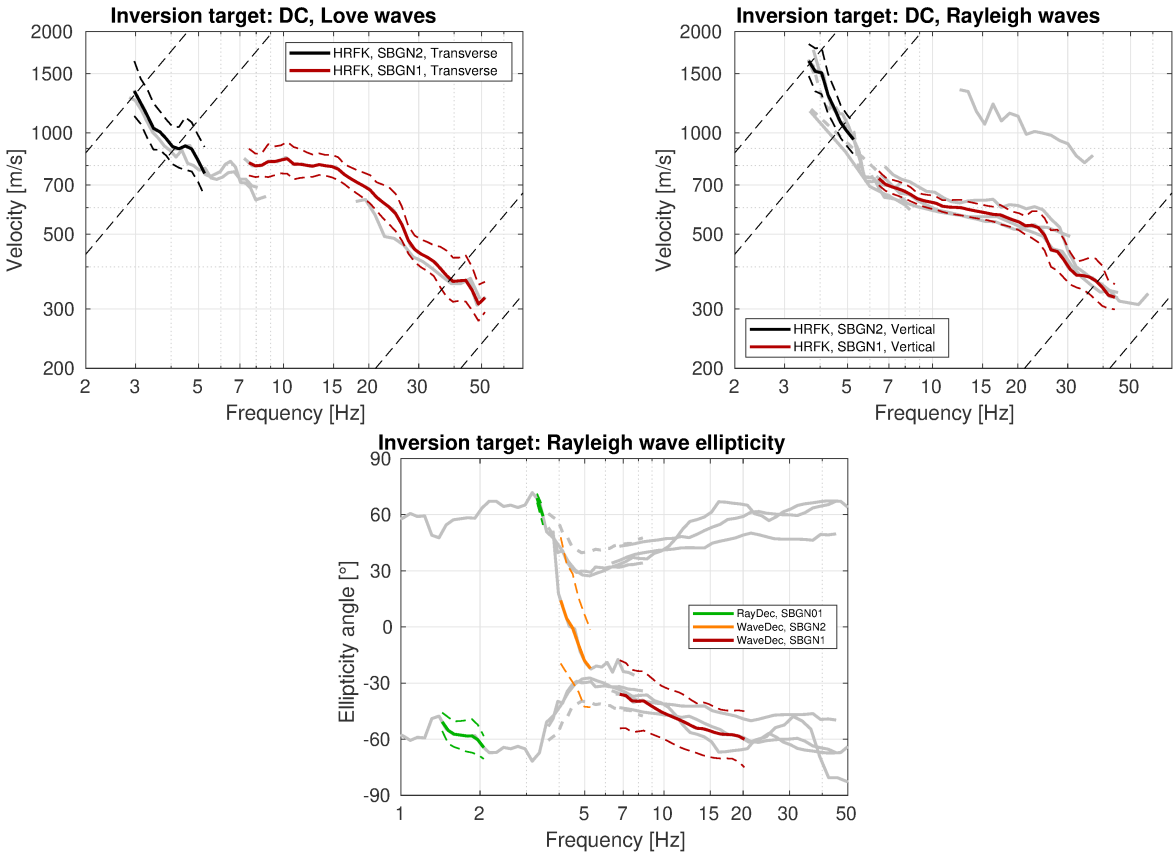

Figure 13: Overview of the dispersion (top) and ellipticity angle (bottom) curves used as targets for the different inversions.

Table 2: List of the different data curves used as target in the different inversions.

Array	Method	Wave type	Mode	Curve type	Frequency range [Hz]
2	HRFK (T)	Love	fundamental	dispersion	2.96 - 5.26
1	HRFK (T)	Love	fundamental	dispersion	7.54 - 51.4
2	HRFK (V)	Rayleigh	fundamental	dispersion	3.65 - 5.26
1	HRFK (V)	Rayleigh	fundamental	dispersion	6.46 - 44.0
	RayDec (SBGN01)	Rayleigh	fundamental	ellipticity angle (-)	1.43 - 2.07
	RayDec (SBGN01)	Rayleigh	fundamental	ellipticity angle (+)	3.29 - 3.47
2	WaveDec	Rayleigh	fundamental	ellipticity angle	4.05 - 5.26
1	WaveDec	Rayleigh	fundamental	ellipticity angle	6.80 - 20.3

4.2 Inversion parameterization

For the inversion, seven different parameterizations have been used in total. The first six had free values of the depths and velocities of the different layers, ranging from four to eight layers (including half-space). The last parameterization had fixed layer depths and consisted of 20 layers in total. The main interface depths resulting from the 8-layer inversion were used in the fixed-layer approach. The P-wave velocities were allowed to vary up to 5000 m/s. The S-wave velocities were allowed to range from 50 to 3500 m/s. The deepest layers were parameterized to range to a depth of 150 m maximum. The density was fixed to 2 300 kg/m^3 for the lowest layer, to 1 900 kg/m^3 for the superficial layer (or the first three layers in the fixed-layer case) and to 2 100 kg/m^3 for all other layers. No low-velocity zones were allowed.

4.3 Inversion results

We performed seven inversions with different parameterizations for the subsurface model. For each parameterization, 20 different runs were performed, but only the one giving the best minimum misfit was kept. In Table 3, the obtained minimum misfit values for these inversions are shown. Each inversion run produced around 150 000 total models in order to assure a good convergence of the solution, except for the 4-layer and 3-layer inversions, where 100 000 and 50 000 generated models were sufficient, respectively. The results of the inversions SBGN3l to SBGNfix are shown in Figs 14 - 20.
The different inversions with more than 4 layers yield similar misfit values and fit the data in a comparable way. Especially the 3-layer inversion yields higher misfit values than the other inversions. For the 4-layer case, it is slightly increased. Using the fixed-depth approach, the minimum misfit was also higher, probably because the interface depths were fixed at non-optimum depths.

Table 3: List of inversions

Inversion	Number of layers	Number of models	Minimum misfit
SBGN3l	3	50 030	0.930
SBGN4l	4	100 028	0.823
SBGN5l	5	150 004	0.780
SBGN6l	6	150 044	0.743
SBGN7l	7	150 001	0.749
SBGN8l	8	150 029	0.751
SBGNfix	20	150 009	0.799

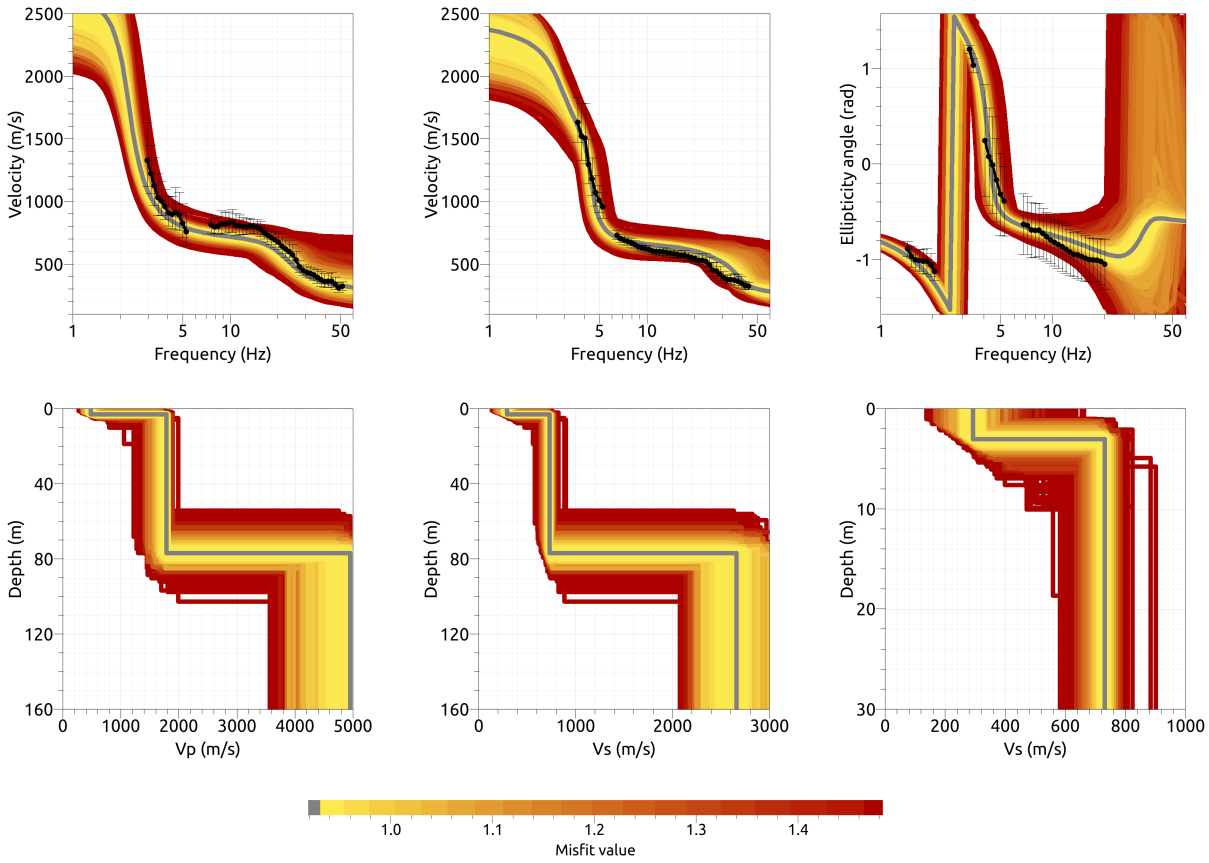

Figure 14: Inversion SBGN3l. Top line: Dispersion curves for Love waves (left) and Rayleigh waves (center) and Rayleigh wave ellipticity angle (right) of the respective fundamental modes. The black dots indicate the data points used for the inversion, the gray line indicates the best-fitting model. Bottom line: P-wave velocity profiles (left), S-wave velocity profiles (center and zoom on the upper 30 m on the right). All generated models are plotted on top of each other in the color corresponding to the respective misfit value.

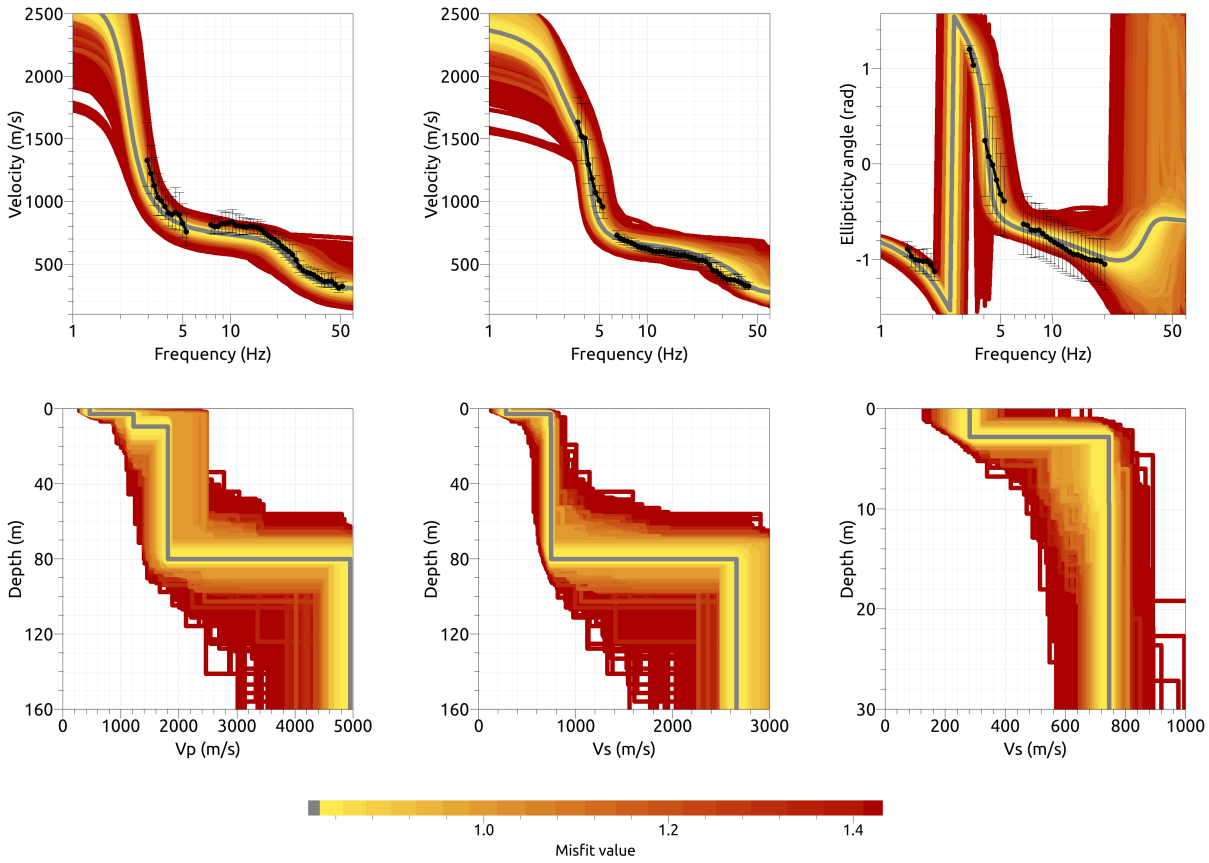

Figure 15: Inversion SBGN4l. Top line: Dispersion curves for Love waves (left) and Rayleigh waves (center) and Rayleigh wave ellipticity angle (right) of the respective fundamental modes. The black dots indicate the data points used for the inversion, the gray line indicates the best-fitting model. Bottom line: P-wave velocity profiles (left), S-wave velocity profiles (center and zoom on the upper 30 m on the right). All generated models are plotted on top of each other in the color corresponding to the respective misfit value.

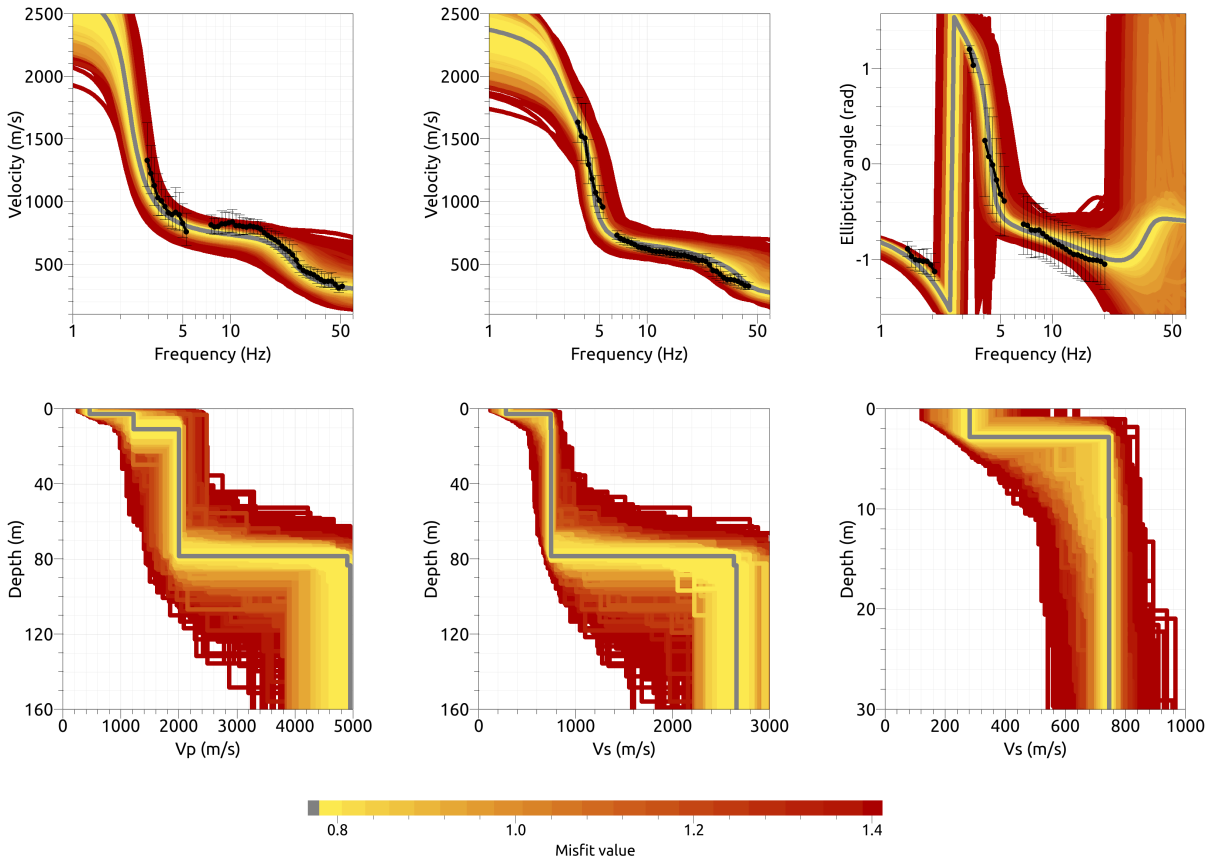

Figure 16: Inversion SBGN5l. Top line: Dispersion curves for Love waves (left) and Rayleigh waves (center) and Rayleigh wave ellipticity angle (right) of the respective fundamental modes. The black dots indicate the data points used for the inversion, the gray line indicates the best-fitting model. Bottom line: P-wave velocity profiles (left), S-wave velocity profiles (center and zoom on the upper 30 m on the right). All generated models are plotted on top of each other in the color corresponding to the respective misfit value.

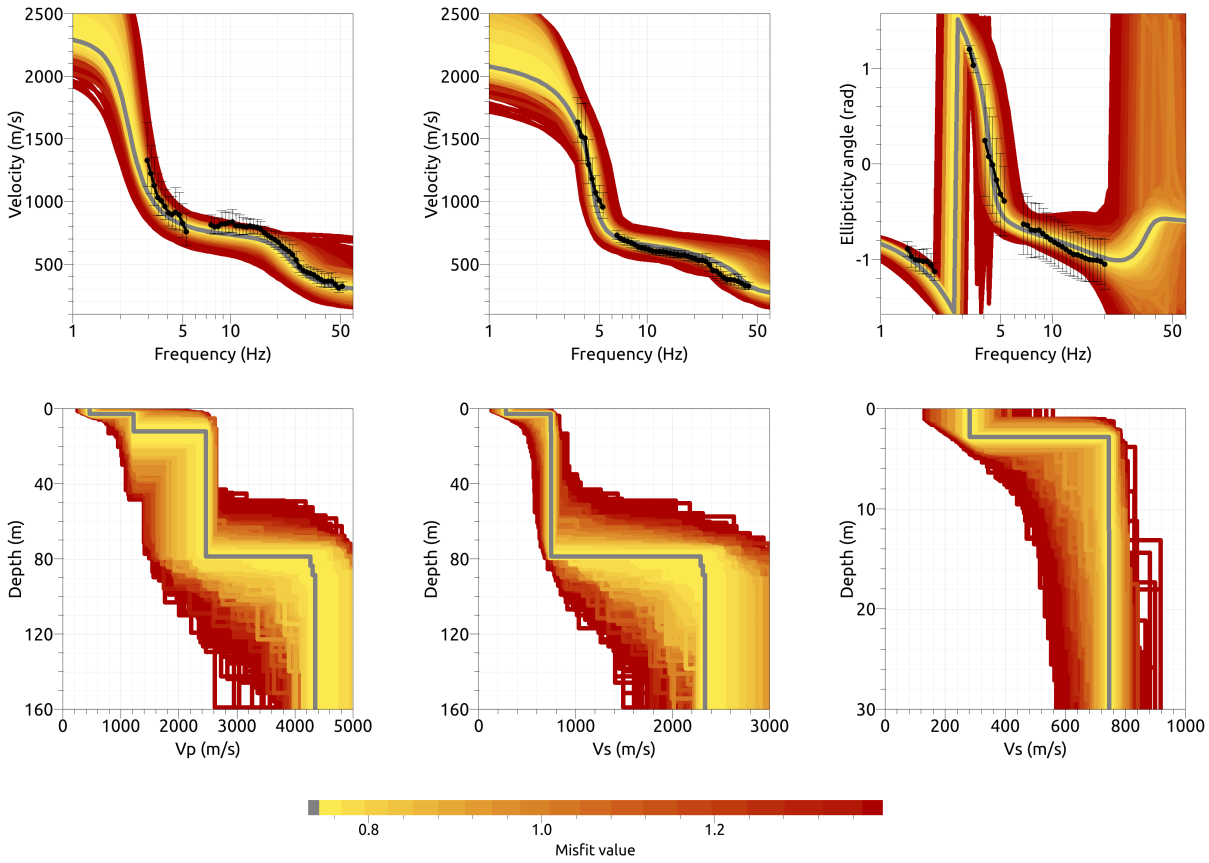

Figure 17: Inversion SBGN6l. Top line: Dispersion curves for Love waves (left) and Rayleigh waves (center) and Rayleigh wave ellipticity angle (right) of the respective fundamental modes. The black dots indicate the data points used for the inversion, the gray line indicates the best-fitting model. Bottom line: P-wave velocity profiles (left), S-wave velocity profiles (center and zoom on the upper 30 m on the right). All generated models are plotted on top of each other in the color corresponding to the respective misfit value.

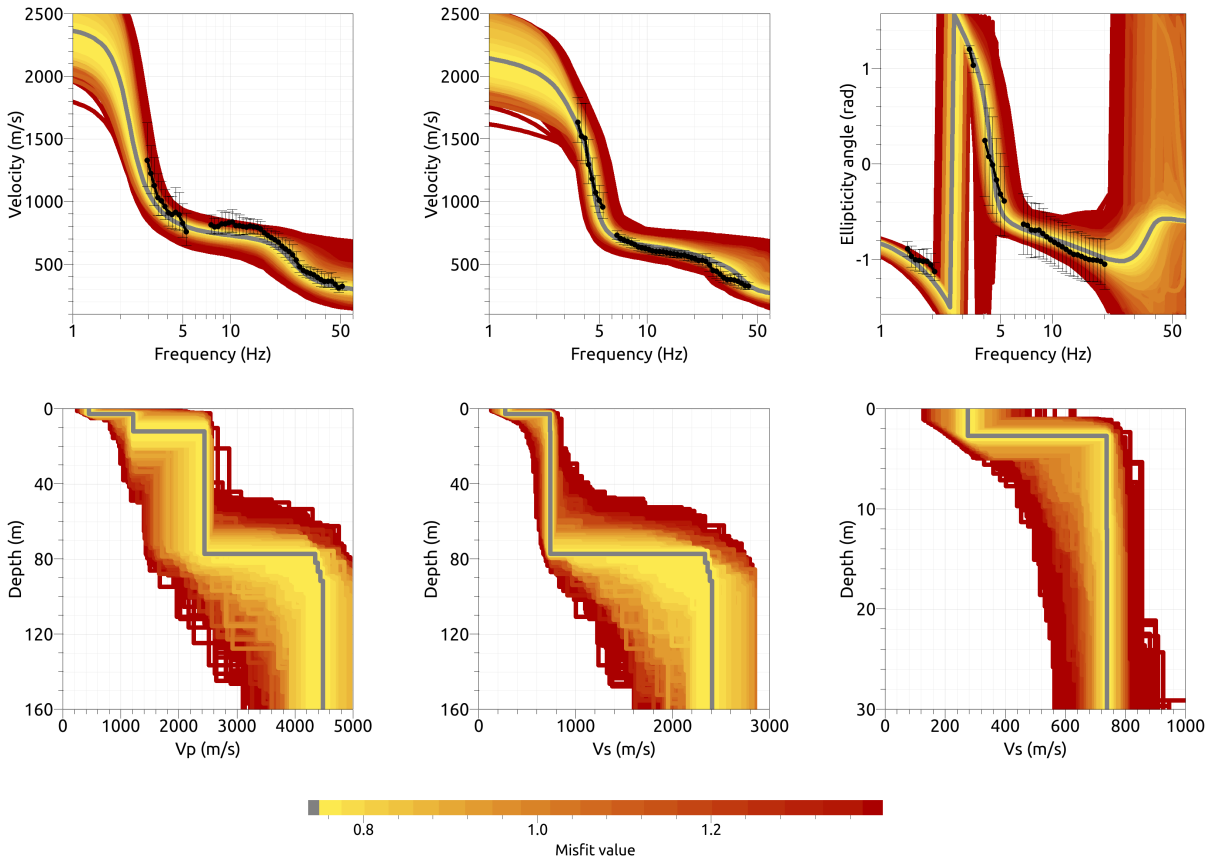

Figure 18: Inversion SBGN7l. Top line: Dispersion curves for Love waves (left) and Rayleigh waves (center) and Rayleigh wave ellipticity angle (right) of the respective fundamental modes. The black dots indicate the data points used for the inversion, the gray line indicates the best-fitting model. Bottom line: P-wave velocity profiles (left), S-wave velocity profiles (center and zoom on the upper 30 m on the right). All generated models are plotted on top of each other in the color corresponding to the respective misfit value.

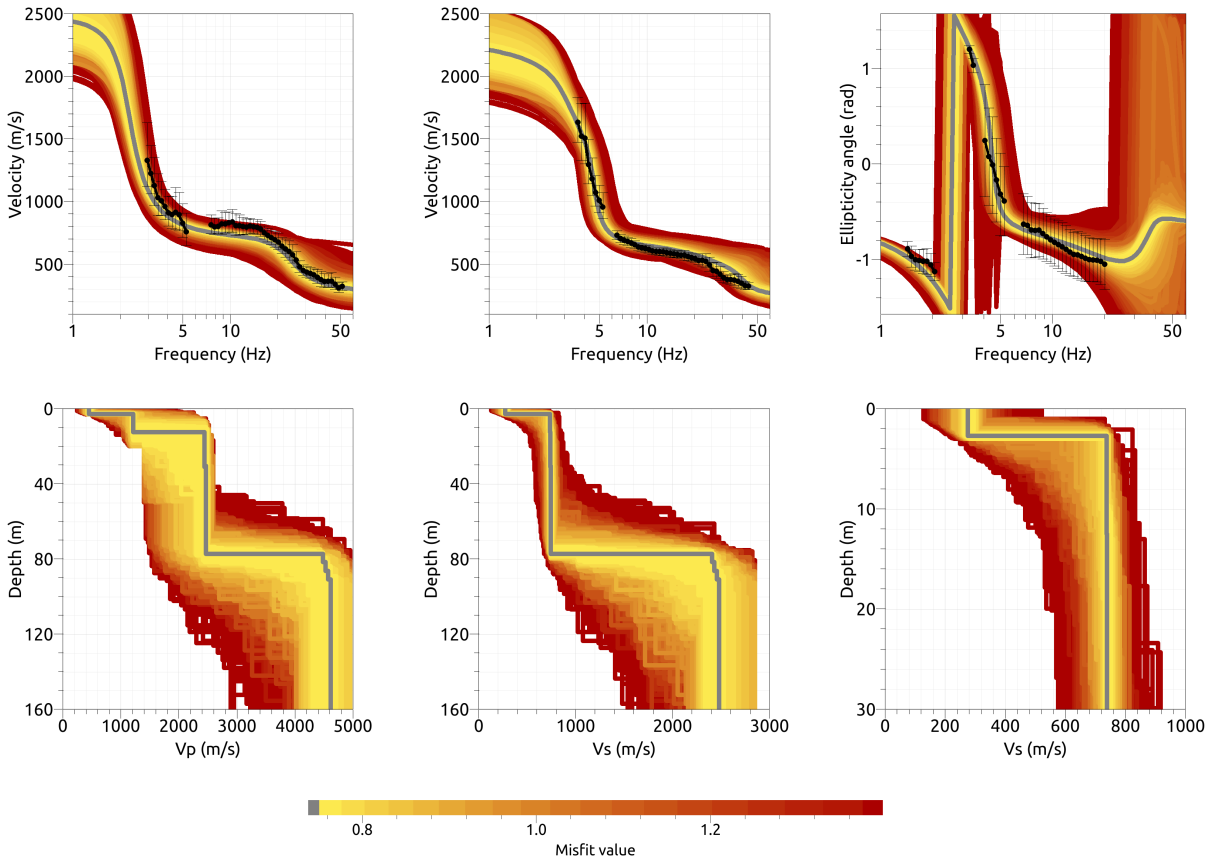

Figure 19: Inversion SBGN8l. Top line: Dispersion curves for Love waves (left) and Rayleigh waves (center) and Rayleigh wave ellipticity angle (right) of the respective fundamental modes. The black dots indicate the data points used for the inversion, the gray line indicates the best-fitting model. Bottom line: P-wave velocity profiles (left), S-wave velocity profiles (center and zoom on the upper 30 m on the right). All generated models are plotted on top of each other in the color corresponding to the respective misfit value.

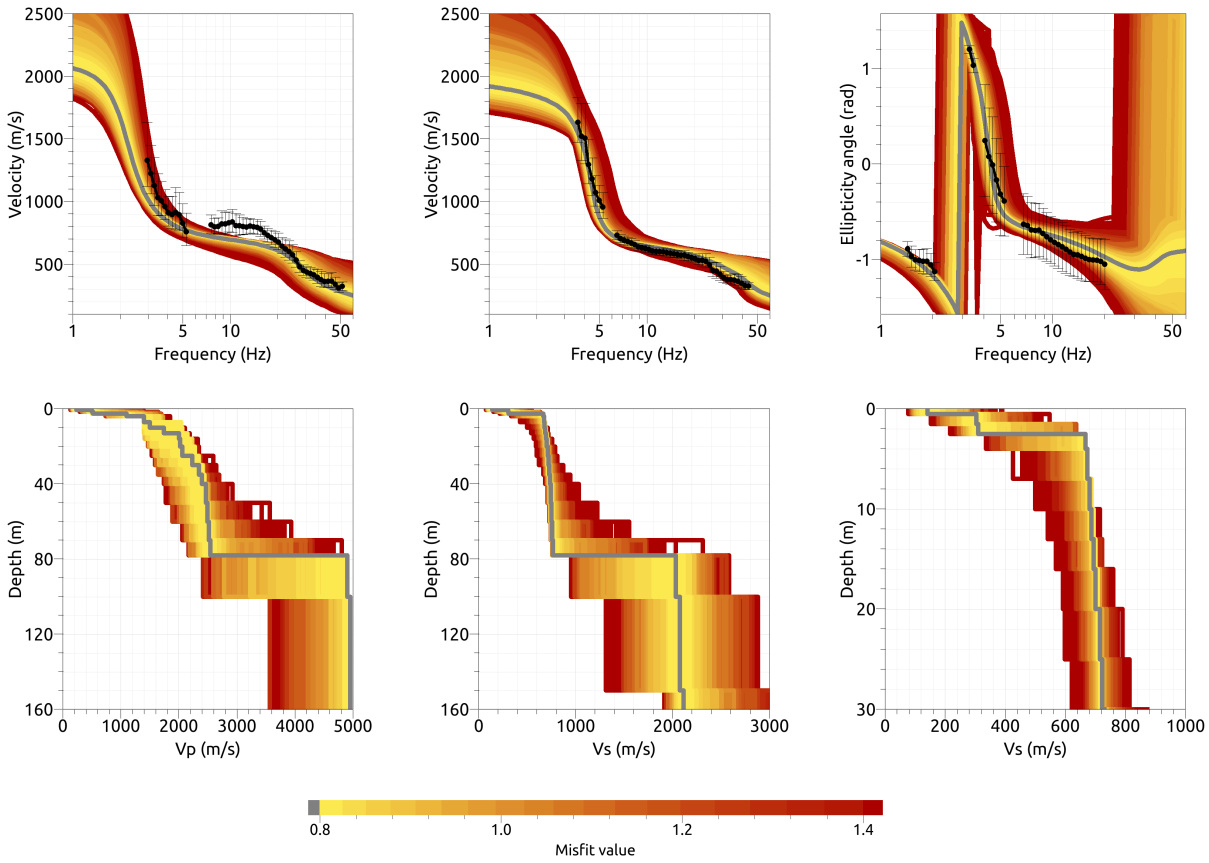

Figure 20: Inversion SBGNfix. Top line: Dispersion curves for Love waves (left) and Rayleigh waves (center) and Rayleigh wave ellipticity angle (right) of the respective fundamental modes. The black dots indicate the data points used for the inversion, the gray line indicates the best-fitting model. Bottom line: P-wave velocity profiles (left), S-wave velocity profiles (center and zoom on the upper 30 m on the right). All generated models are plotted on top of each other in the color corresponding to the respective misfit value.

4.4 Overview of the inversion result

The best-fitting models of the inversions SBGN3l-SBGNfix are shown in Fig. 21. All models show similar main features, even the three-layer case. The superficial layer with a thickness of 2.5 to 3.0 m has a shear-wave velocity of about 280 m/s, followed by a layer with a velocity of between 730 and 750 m/s down to about 77 to 80 m, where the seismic bedrock with velocities of over 2000 m/s is found.
Inversions with more layers tend to smoothen the transitions between the different formations.
All inversions except for the three-layer inversion were accepted as valid models for the underground structure. The V_{S30} value for these inversions ranges from 606.9 to 646.1 m/s (average value 638.1 $\pm$ 15.4 m/s). This corresponds to soil class B in both EC8 and SIA261.

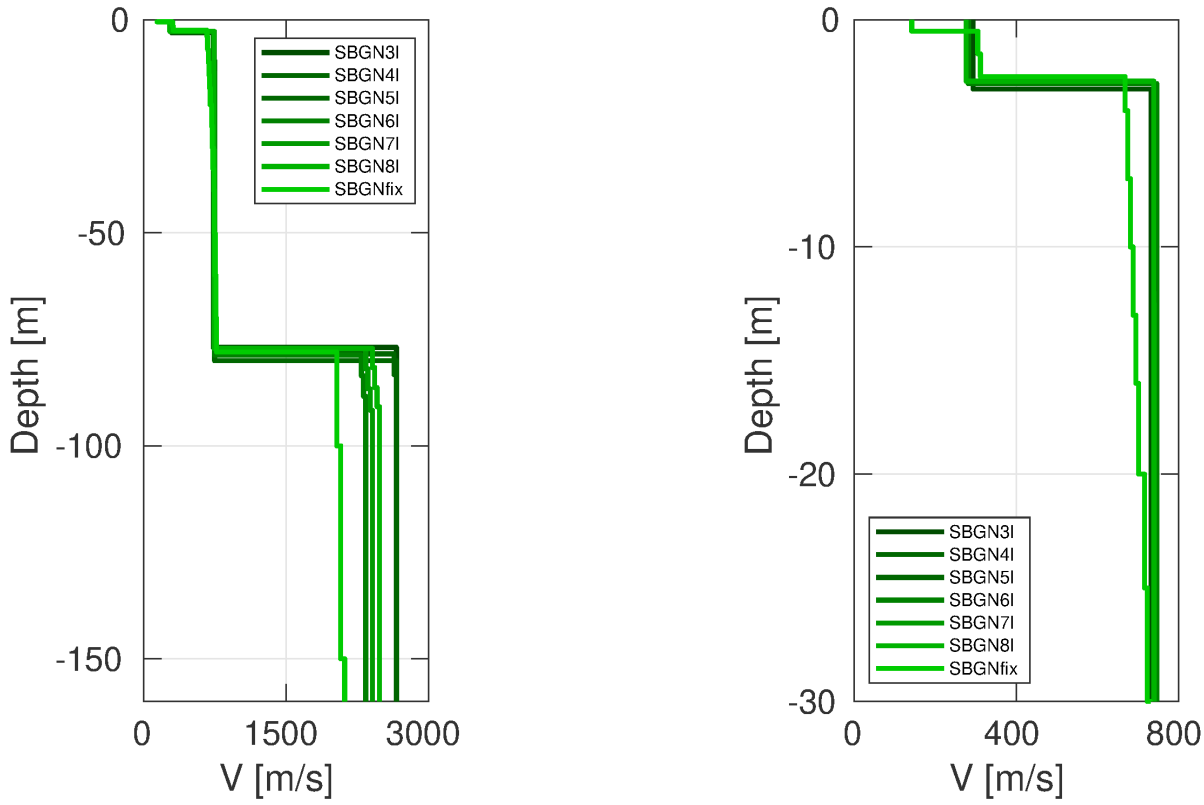

Figure 21: Overview of shear-wave velocity profiles of the best-fitting models of all inversions (left) and a zoom on the shallow part (right).

4.5 Site amplification

In Fig. 22, the theoretical amplification function for the best models resulting from the six selected inversions is compared with the empirical amplification. The empirical amplification for station SBGN is based on 47 events so far. The amplification for the inversion models is in good agreement with the empirical amplification around the peak frequency at around 2.5 Hz, even if the amplitudes are different. At higher frequencies, the empirical amplification is relatively flat between 5 and 20 Hz. This might be a sign for edge-generated surface waves that affect the site and are not included in the modeling of vertically propagating S-waves.

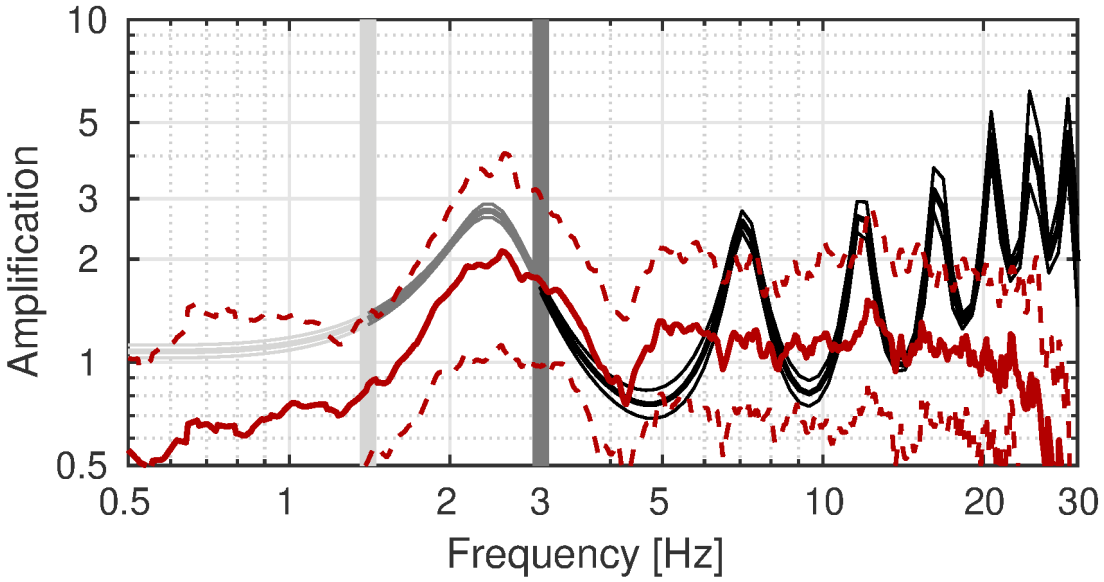

Figure 22: Comparison between the modeled amplification for the final set of best models of the different inversions (SBGN4l-SBGNfix; in gray to black, with standard deviation) and the empirical amplification measured at station SBGN (red, with standard deviation). The vertical light and dark grey bars correspond to the lowest frequency of the ellipticity and dispersion curves, respectively.

4.6 Quarter-wavelength representation

The quarter-wavelength velocity approach (Joyner et al., 1981) provides, for a given frequency, the average velocity at a depth corresponding to 1/4 of the wavelength of interest. It is useful to identify the frequency limits of the experimental data (the minimum frequency of the dispersion curve used in the inversion is 2.96 Hz, the minimum frequency used for the ellipticity inversion 1.43 Hz). The results using this proxy show that the dispersion curves constrain the profiles down to only about 60 m, but down to over 200 m using the ellipticity information (Fig. 23). Moreover, the quarter wavelength impedance-contrast introduced by Poggi et al. (2012) is also displayed in the figure. It corresponds to the ratio between two quarter-wavelength average velocities, respectively from the top and the bottom part of the velocity profile, at a given frequency (Poggi et al., 2012). This curve shows a strong contrast at the fundamental frequency of the site.

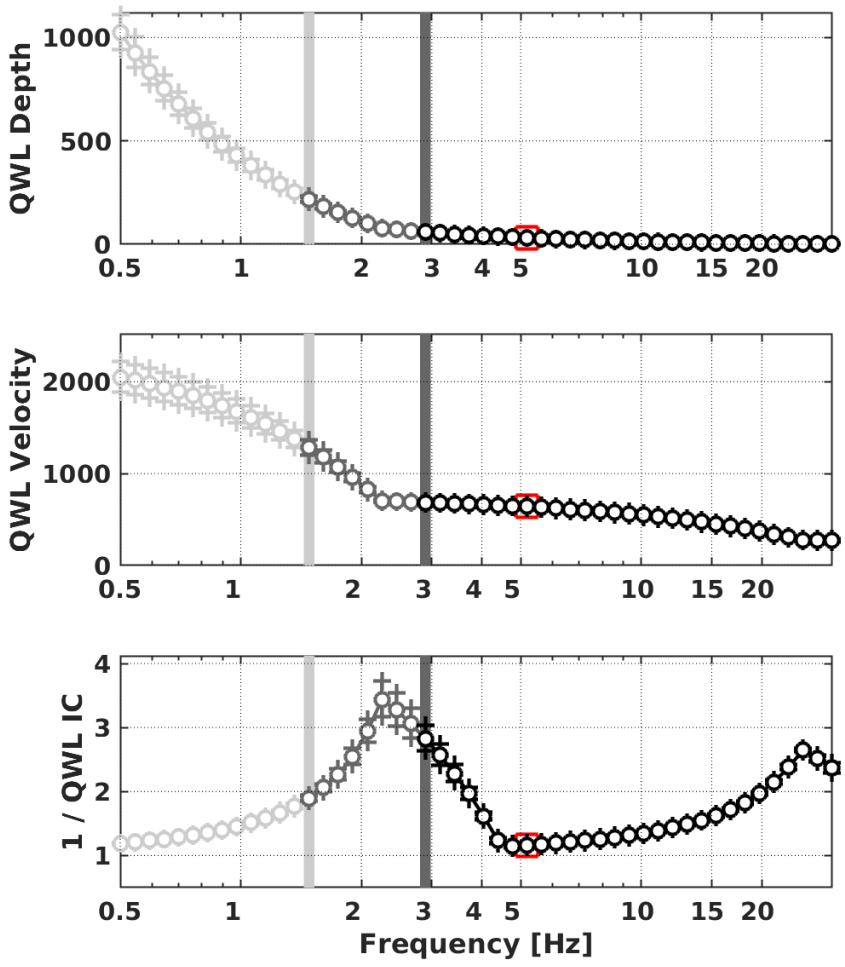

Figure 23: Quarter wavelength representation of the velocity profile for the best models of the inversions (top: depth, center: velocity, bottom: inverse of the impedance contrast). The black curves are constrained by the dispersion curves, the light grey curves are not constrained by the data. The red square corresponds to V_{S30}.

5 Conclusion

We performed a passive array measurement with two arrays to characterize the soil underneath station SBGN in Bergün/Bravuogn (GR), located on the transition zone between alluvial deposits and moraine.
The dispersion curves for Love and Rayleigh waves could be measured over a wide frequency range, from around 2.9 to 51.7 Hz for Love waves and from 3.6 to 41.5 Hz for Rayleigh waves. The fundamental ellipticity peak frequency is around 3 Hz.
The joint inversion of Love and Rayleigh wave dispersion curves and the Rayleigh wave ellipticity angle showed that the structure can be explained by models with interfaces at around 2.5 m and 80 m depth. The latter value corresponds to H800. The V_{S30} of the best models is about 638 m/s, corresponding to soil class B in both EC8 and SIA261.

Acknowledgements

The authors thank Marthe Faber and David Farsky for their help during the array measurements.

References

Aki, K. (1957). Space and time spectra of stationary stochastic waves, with special reference to microtremors. *Bull. Earthquake Res. Inst. Tokyo Univ.*, 35:415–456.

Bettig, B., Bard, P.-Y., Scherbaum, F., Riepl, J., Cotton, F., Cornou, C., and Hatzfeld, D. (2001). Analysis of dense array noise measurements using the modified spatial auto-correlation method (SPAC): application to the Grenoble area. *Boll. Geof. Teor. Appl.*, 42:281–304.

Burjánek, J., Gassner-Stamm, G., Poggi, V., Moore, J. R., and Fäh, D. (2010). Ambient vibration analysis of an unstable mountain slope. *Geophys. J. Int.*, 180:820–828.

Burjánek, J., Moore, J. R., Molina, F. X. Y., and Fäh, D. (2012). Instrumental evidence of normal mode rock slope vibration. *Geophys. J. Int.*, 188:559–569.

Fäh, D., Wathelet, M., Kristekova, M., Havenith, H., Endrun, B., Stamm, G., Poggi, V., Burjanek, J., and Cornou, C. (2009). Using ellipticity information for site characterisation. NERIES deliverable JRA4 D4, available at http://www.neries-eu.org.

Hobiger, M., Bard, P.-Y., Cornou, C., and Le Bihan, N. (2009). Single station determination of Rayleigh wave ellipticity by using the random decrement technique (RayDec). *Geophys. Res. Lett.*, 36.

Joyner, W. B., Warrick, R. E., and Fumal, T. E. (1981). The effect of Quaternary alluvium on strong ground motion in the Coyote Lake, California, earthquake of 1979. *Bull. Seismol. Soc. Am.*, 71(4):1333–1349.

Maranò, S., Reller, C., Loeliger, H.-A., and Fäh, D. (2012). Seismic waves estimation and wavefield decomposition: Application to ambient vibrations. *Geophys. J. Int.*, 191:175–188.

Poggi, V., Edwards, B., and Fäh, D. (2012). Characterizing the Vertical-to-Horizontal ratio of ground motion at soft-sediment sites. *Bull. Seismol. Soc. Am.*, 102(6):2741–2756.

Poggi, V. and Fäh, D. (2010). Estimating Rayleigh wave particle motion from three-component array analysis of ambient vibrations. *Geophys. J. Int.*, 180:251–267.